Lifetime measurements to investigate γ softness and shape coexistence in ^{102}Mo

A. Esmaylzadeh,[1,*] V. Karayonchev,[1] K. Nomura,[2] J. Jolie,[1] M. Beckers,[1] A. Blazhev,[1] A. Dewald,[1] C. Fransen,[1] R.-B. Gerst,[1] G. Häfner,[1,3] A. Harter,[1] L. Knafla,[1] M. Ley,[1] L. M. Robledo,[4,5] R. Rodríguez-Guzmán,[6] and M. Rudigier[7]

[1]*Universität zu Köln, Institut für Kernphysik, D-50937 Köln, Germany*
[2]*Department of Physics, Faculty of Science, University of Zagreb, 10000 Zagreb, Croatia*
[3]*Université Paris-Saclay, IJCLab, CNRS/IN2P3, F-91405 Orsay, France*
[4]*Departamento de Física Teórica, Universidad Autónoma de Madrid, E-28049 Madrid, Spain*
[5]*Center for Computational Simulation, Universidad Politécnica de Madrid, Campus de Montegancedo, Boadilla del Monte, E-28660 Madrid, Spain*
[6]*Physics Department, Kuwait University, 13060 Kuwait, Kuwait*
[7]*Technische Universität Darmstadt, Insitut für Kernphysik, D-64289 Darmstadt, Germany*

(Received 29 September 2021; accepted 7 December 2021; published 15 December 2021)

Lifetimes of low-spin excited states in ^{102}Mo populated in a ^{100}Mo(^{18}O, ^{16}O) ^{102}Mo two-neutron transfer reaction were measured using the recoil-distance Doppler-shift technique at the Cologne FN Tandem accelerator. Lifetimes of the 2_1^+, 4_1^+, 6_1^+, 0_2^+, 2_γ^+, 3_γ^+ states and one upper limit for the lifetime of the 4_γ^+ state were obtained. The energy levels and deduced electromagnetic transition probabilities are compared with those obtained within the mapped interacting boson model framework with microscopic input from Gogny mean-field calculations. With the newly obtained signatures a more detailed insight in the γ softness and shape coexistence in ^{102}Mo is possible and discussed in the context of the $Z \approx 40$ and $N \approx 60$ region. The nucleus of ^{102}Mo follows the γ soft trend of the Mo isotopes. The properties of the 0_2^+ state indicate, in contrast with the microscopic predictions, shape coexistence which also occurs in other $N = 60$ isotones.

DOI: 10.1103/PhysRevC.104.064314

I. INTRODUCTION

Nuclei with proton or neutron number close to the magic numbers tend to exhibit a spherical ground state. Moving away from a closed shell results in an increase of collectivity. Compared with the usual gradual process, this development is strictly different in the $A \approx 100$ region, especially for the neutron-rich Zr and Sr isotopes [1,2]. They undergo a rapid change from spherical to a deformed type of structure going from $N = 58$ to $N = 60$ (see Fig. 1). The proton subshell closures at $Z = 38, 40$ ($\pi p_{3/2}$ and $\pi p_{1/2}$) as well as the neutron subshell closures at $N = 50$, 56, 58 ($\nu g_{9/2}$, $\nu d_{5/2}$, and $\nu s_{1/2}$) lead to a low-energy structure of a semimagic nucleus for the $N = 50$–58 ($^{88-96}$Sr) strontium and ($^{90-98}$Zr) zirconium isotopes. The ruthenium isotopes ($Z = 44$) show a rather smooth transition from a more spherical shape to a deformed one. The more neutron-rich ruthenium isotopes show a triaxial behavior, where the maximum triaxiality is reached around neutron number $N = 66$ and 68 (^{110,112}Ru) [3–6]. The molybdenum isotopes are centered between the ruthenium, with some degree of γ softness, and the zirconium isotopes, showing a rapid change from a spherical to a deformed structure. This creates a challenge for theoretical models to accurately describe the interplay of different nuclear structure phenomena dominant in this region. The semimagic ^{92}Mo ($N = 50$) is spherical [7], where the low-energy excited states are formed by the interaction between protons in the $\pi g_{9/2}$ orbital and the neutrons in the $\nu g_{7/2}$ orbital. The energy of the first-excited 2_1^+ state decreases with increasing neutron numbers after $N = 56$, while the $B(E2; 2_1^+ \rightarrow 0_1^+)$ strengths shows an opposite behavior (see Fig. 1). This suggests that, with increasing neutron number, the influence of collective motion becomes stronger [8]. Compared with the Sr and Zr isotopes, the molybdenum isotopes show a less rapid shape evolution where the emergence of triaxiality could play a major role [23]. Different experimental evidence for triaxiality in neutron-rich even-even molybdenum isotopes was reported [8,22,24,25]. The γ band with its 2_γ^+ state bandhead is strongly related to the triaxial motion [26] where the potential-energy surface minimum is located between $\gamma = 0^\circ$ (prolate shape) and $\gamma = 60^\circ$ (oblate shape). The relative position of the 2_γ^+ states with respect to the 4_1^+ state changes at $N = 54$ and again at $N = 60$ with the 2_γ^+ states being lower in between. Two important models, that discuss this kind of low-lying 2_γ^+ states and the triaxial shape, are the Davydov-Filippov rigid triaxial rotor model [27–29] and the Wilets-Jean γ unstable rotor model [30]. In the Wilets-Jean γ unstable rotor model (hereafter γ soft model), the energies of the 4_1^+ and 2_γ^+ states are degenerate, while the Davydov-Filippov model predicts the 2_γ^+ at a lower energy than the 4_1^+ state at the maximum of triaxiality at $\gamma = 30^\circ$. The similarities of the models require the use of further parameters to distinguish between them. Therefore, the energy staggering of the γ-band can be considered, which is opposite for both models [26,31]. In the prediction of the γ-soft model, the states corresponding

*aesmaylzadeh@ikp.uni-koeln.de

to the γ band are clustered as (2^+_γ), $(3^+_\gamma, 4^+_\gamma)$ and $(5^+_\gamma, 6^+_\gamma)$ in comparison to a $(2^+_\gamma, 3^+_\gamma)$, $(4^+_\gamma, 5^+_\gamma)$ clustering structure in the rigid triaxial rotor (Davydov-Filippov model) [32].

Further insights can be obtained by the observation of the second 0^+_2 state, which can be an indicator for β vibration or a possible coexisting shape [33,34]. The 0^+_2 state for the molybdenum isotopes starts at 1.7 MeV in ^{94}Mo, has its minimum for ^{100,102}Mo (with both almost at the same energy around 700 keV), and increases its energy to 1 MeV for ^{106}Mo. In ^{98}Mo the 0^+_2 state is the first-excited state and shape coexistence has been confirmed by different works [35,36].

In the present study, low-lying states of ^{102}Mo were observed and lifetimes were determined to further investigate the describe phenomena in this interesting region of the nuclear chart. The obtained lifetimes and the deduced transition probabilities of these states are powerful tools to get a detailed distinction of different models and their interpretation. The results are compared with the proton-neutron version of the interacting boson model (IBM-2) with microscopic input from the self-consistent mean-field approximation based on the Gogny-D1M energy density functional discussed in Ref. [37].

II. EXPERIMENT

The nucleus of interest was populated using a two-neutron transfer reaction, i.e., ^{100}Mo(^{18}O, ^{16}O) ^{102}Mo. An average beam current of $\approx$1 pnA with an energy of 52 MeV was provided by the Cologne 10 MV FN-Tandem accelerator. The highly enriched (99.7%) ^{100}Mo target with a thickness of 1 mg/cm^2 and a 1.9 mg/cm^2 thick natural magnesium backing was stretched inside the Cologne Plunger device [38]. In addition, a natural magnesium stopper foil was stretched in parallel to the target and acted as a stopper for the ejectiles. To detect the γ rays produced in the reaction, eleven high-purity germanium (HPGe) detectors were used forming two rings (backward and forward) around the target chamber. The six forward detectors were positioned at an angle of 45°, whereas the five backward detectors were placed at an angle of 142° with respect to the beam direction. Similar to previous experiments using the same configuration [39–41], six solar cells were installed at backward angles to detect the backscattered light recoiling fragments. To apply the recoil distance Doppler-shift (RDDS) technique, twelve target-to-stopper distances (15, 29, 44, 64, 84, 114, 214, 414, 714, 1114, 1814, and 2414 μm) were measured in approximately 12 days of beam time. The absolute values of these distances were obtained by using the capacitive method which is described in Refs. [38,42] and verified by different lifetimes of the Coulomb excitation of ^{100}Mo. The origin of the uncertainty arises from the fit of the data points using the capacitive method but also from the different used lifetimes of ^{100}Mo, where each lifetime obtains a different so-called zero point. Therefore, the uncertainty of the zero-point determination was calculated to be 5 μm. The velocity of the recoiling ^{102}Mo was determined using the shifted and unshifted components of the most intensive transitions and results in $v/c = 1.83(10)\%$. A particle spectrum and a particle-gated γ spectrum of the shortest distance is shown in Fig. 2. In addition, a partial level scheme is shown that was built using the information given in the spectrum with spins and parities of the states taken from the literature [15]. The dashed lines in Fig. 2(a) indicate γ-ray transitions that were not observed due to their low intensity. The observation limit is about 2% relative to the $2^+_1 \rightarrow 0^+_1$ transition and the intensities are summarized in Table I. The strongest γ rays belong to ^{100}Mo and ^{102}Mo. An exclusion of the Coulomb excitation channel (^{100}Mo) with the particle gate was not possible due to the energy and angular struggling of the recoiling ^{18}O and ^{16}O particles as well as the angular coverage of the solar cells.

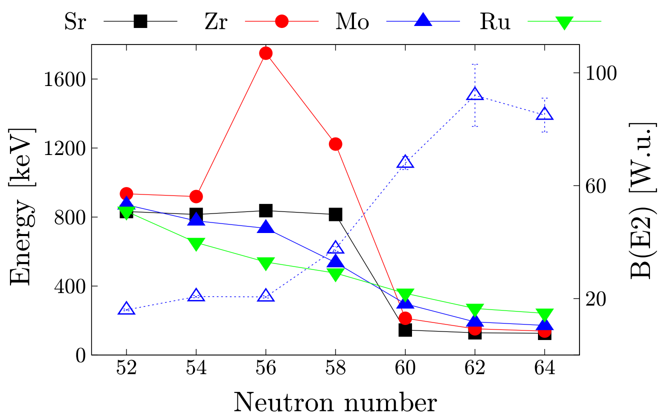

FIG. 1. The energies of the first-excited 2^+_1 states (filled symbols) for Sr ($Z = 38$), Zr ($Z = 40$), Mo ($Z = 42$), and Ru ($Z = 44$) isotopes with $N = 52$–64. Data are taken from the Nuclear Data Sheets [9–18]. Also the $B(E2; 2^+_1 \rightarrow 0^+_1)$ for the Mo isotopes are shown (open symbols) where the values are taken from Refs. [13–15,19–22].

III. ANALYSIS

The lifetimes of the 2^+_1, 4^+_1, 6^+_1, 0^+_2, 2^+_γ, 3^+_γ states and an upper limit for the lifetime of the 4^+_γ state have been determined using the Bateman equations [44] to analyze the recoil distance Doppler-shift data. In addition, the well-established differential decay curve method (DDCM) [45] has been used, which has some advantages like the detection of certain systematic errors. It uses only experimental accessible values and no assumption on the $R(t)$ curve shape are used. Another advantages in contrast to the Bateman equations is the use of relative distances, which eliminates the uncertainty of the absolute distance determination. Only particle-gated single γ-ray spectra were used to analyze the data, where γ-γ coincidences could not be employed due to lack of statistics. A detailed description of both methods is given in Ref. [38]. Due to the low statistics, for the 4^+_γ state the method explained in Refs. [40,46] was used to obtain the lifetime. The summed spectra of all distances j was used in combination with the following solution of the Bateman equations [40,46]:

$$R_{\text{sum}} = \frac{\sum_j I^u_j}{\sum_j I^u_j + \sum_j I^s_j} = \sum_j n_j R(t_j), \qquad (1)$$

where I^u_j and I^s_j are the intensities of the unshifted and shifted component, respectively. The normalization factor n_j needs to be obtained for each distance, and t_j corresponds to the

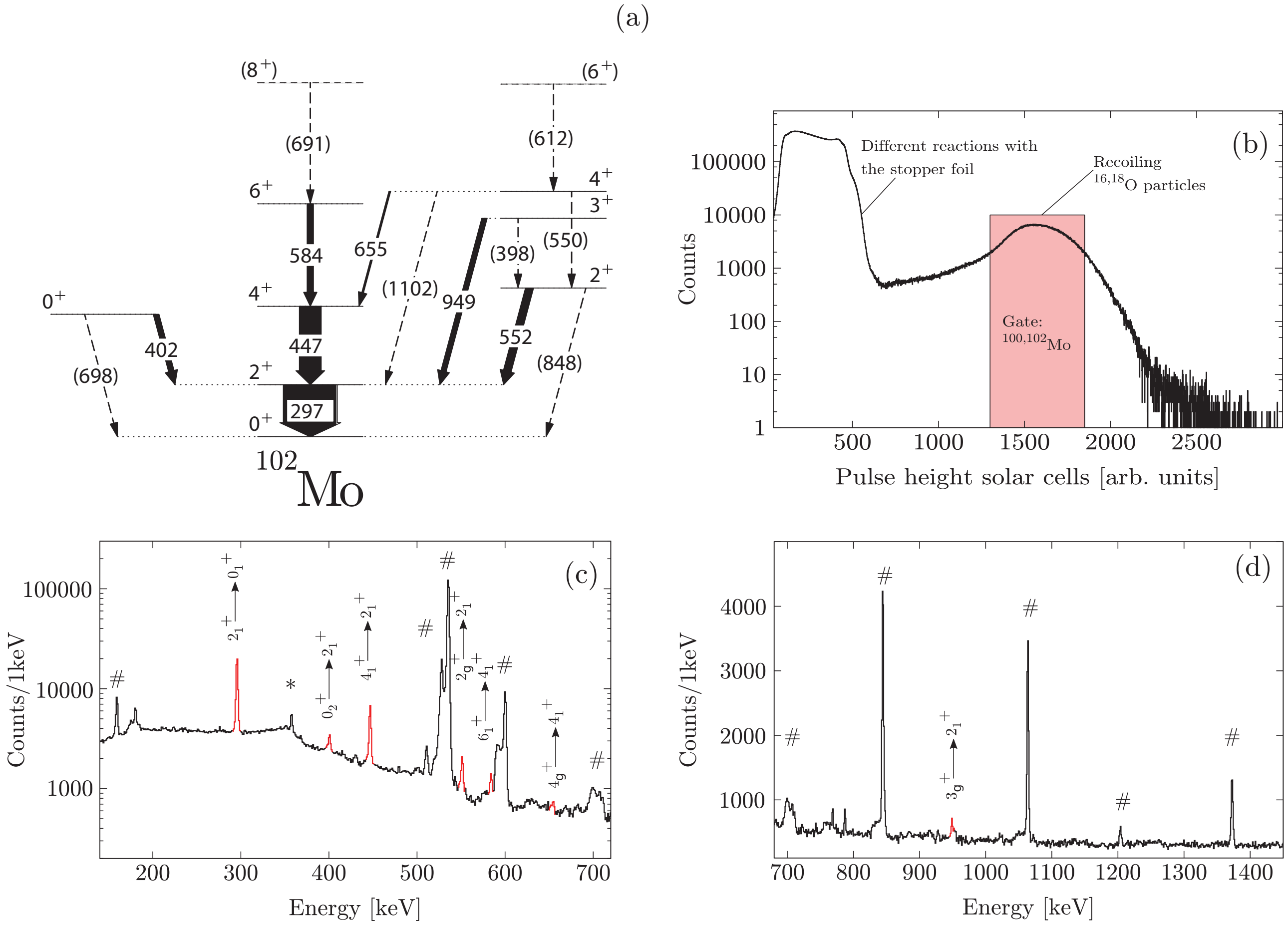

FIG. 2. (a) Partial level scheme of the observed states in ^{102}Mo using the ^{100}Mo(^{18}O, ^{16}O) ^{102}Mo two-neutron transfer reaction. The width of the transition arrows corresponds to the intensities (see Table I) and the dashed lines indicate known transitions not observed in this experiment. (b) The solar cell spectrum of the 15 μm distance. The rectangle shows the gate that has been used for the analysis of ^{102}Mo. (c) Particle gated singles γ-ray spectrum of the backward HPGe detector ring for the shortest distance of 15 μm. The spectrum is shown for the energy range from 120 keV up to 720 keV in which the observed transitions of ^{102}Mo are indicated and colored in red. The transitions marked with # belong to the Coulomb excitation of ^{100}Mo and transitions marked with * stem from ^{104}Ru, populated by the α-transfer reaction channel. Note that the y scale is logarithmic. (d) Same for the energy range 680 up to 1450 keV with a linear y scale.

flight-time of each distance. As discussed in Refs. [39,40] a top-to-bottom approach was used to determine the lifetimes to adjust the feeding pattern for lower-lying states. The uncertainties for the single measurements were determined using a Monte Carlo simulation were all parameters were varied within their uncertainties. The adopted values are calculated using the weighted average of the results. A systematic error of 5% is added which can be caused by different sources, like the opening angle of the detectors, slowing down effects within the target and deorientation effects, especially for $\tau > 100$ ps.

TABLE I. Relative transition intensities observed in the two neutron transfer ^{100}Mo(^{18}O, ^{16}O) ^{102}Mo reaction. The intensities were normalized to the $2^+_1 \rightarrow 0^+_1$ transition and the energies are taken from Ref. [15].

Transition	Transition energy [keV]	Intensity
$2^+_1 \rightarrow 0^+_1$	296.6	100.0(7)
$0^+_2 \rightarrow 2^+_1$	401.9	10.4(14)
$4^+_1 \rightarrow 2^+_1$	447.1	40.3(8)
$2^+_\gamma \rightarrow 2^+_1$	551.6	12.2(15)
$6^+_1 \rightarrow 4^+_1$	584.2	11.5(11)
$4^+_\gamma \rightarrow 4^+_1$	654.6	2.5(20)
$3^+_\gamma \rightarrow 2^+_1$	948.9	5.0(24)

A. The analysis of the 4^+_γ state

The highest observed state in this experiment is the 4^+_γ state. Due to the low population of the state only Eq. (1) could be employed to obtain its lifetime. After the determination of the normalization factors n_j and R_{sum}, a Monte Carlo simulation (with 10^6 iterations) was used to obtain the final lifetime. All the input parameters (n_j, R_{sum}, v/c and the distance) used in the fit are independently varied within their corresponding experimental uncertainty. The resulting lifetime of $\tau_{4^+_\gamma} = 3(1)$ ps has been obtained for which no feeding is assumed. The small intensity is almost at the observation limit and possible unobserved feeders can influence the resulting

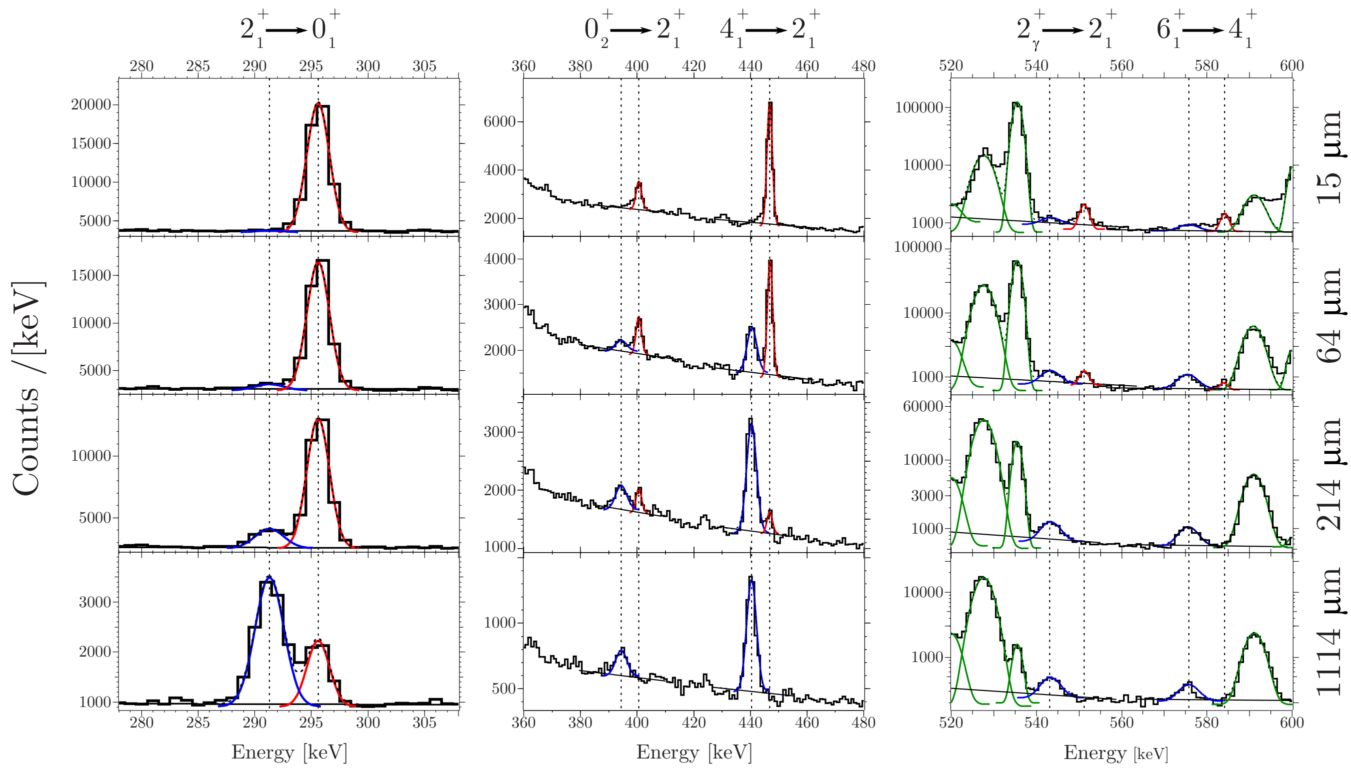

FIG. 3. The evolution of the shifted (blue) and unshifted (red) components in the backward ring for the $2^+_1 \rightarrow 0^+_1$ (left panel), $0^+_2 \rightarrow 2^+_1$ (middle panel), $4^+_1 \rightarrow 2^+_1$ (middle panel), $2^+_\gamma \rightarrow 2^+_1$ (right panel) and $6^+_1 \rightarrow 4^+_1$ (right panel) transitions for four distances, namely 15, 64, 214, and 1114 μm. The solid line indicates the background level and different disturbing peaks were also fit (green). The disturbing transitions, i.e., at 536 and 600 keV with their shifted components belong to ^{100}Mo.

lifetime. To account for these factors a simulation to account for the feeding contribution was performed. A possible feeder is the 6^+_γ state which is indicated in Fig. 2(a). An assumption for the maximum feeding from this state and possible other but unobserved states can be extrapolated from the feeding of the lower-lying states and by the fact that the population of states in transfer reactions is decreasing with increasing spin and excitation energy [39–41]. A realistic amount of feeding contribution would in this case be 20%. In other words, 80% is directly populated through the reaction. For the sake of simplicity, the feeding is modeled by a single hypothetical state with an effective lifetime of 100 ps which is sufficiently long to be considered as a pure long-lived feeding [40,41]. After including the feeding intensity and lifetime in the simulation, a lifetime of $\tau_{4^+_\gamma} = 1(1)$ ps was calculated. The lower limit of the simulation is used as the lower limit of the lifetime [40,41]. This leads to a range of 0–4 ps for the lifetime of this state or an upper limit of $\tau_{4^+_\gamma} < 4$ ps. Although this is only an upper limit, it is important for the lower-lying states (2^+_1, 2^+_γ, and 3^+_γ) to know the feeding contribution of this state.

B. The analysis of the 6^+_1 and 3^+_γ states

The lifetimes of the 6^+_1 and 3^+_γ states were analyzed using the Bateman equations and the differential decay curve method (DDCM) without taking into account unobserved feeding. The mean average of the lifetimes result in $\tau_{6^+_1} = 6.7(7)$ ps and $\tau_{3^+_\gamma} = 5.7(10)$ ps, respectively. The decay curves and the evolution of the shifted and unshifted component for the 6^+_1 state are shown in Figs. 3–5. For the determination of the lifetimes, the $6^+_1 \rightarrow 4^+_1$ transition with 584 keV and the $3^+_\gamma \rightarrow 2^+_1$ transition with 949 keV were used. To investigate possible feeding contributions from higher-lying

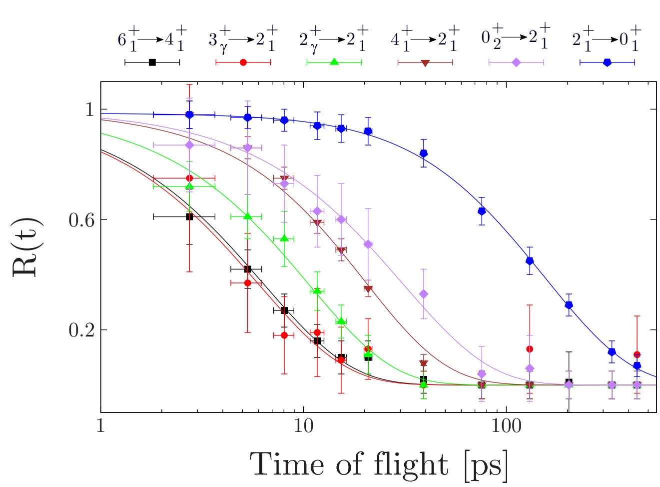

FIG. 4. The decay curves for the lifetimes of the 6^+_1, 3^+_γ, 2^+_γ, 4^+_1, 0^+_2, and 2^+_1 states using the Bateman equations to fit the data of the backward ring at 142°. Note that the x scale is logarithmic. The lifetimes are summarized in Table II.

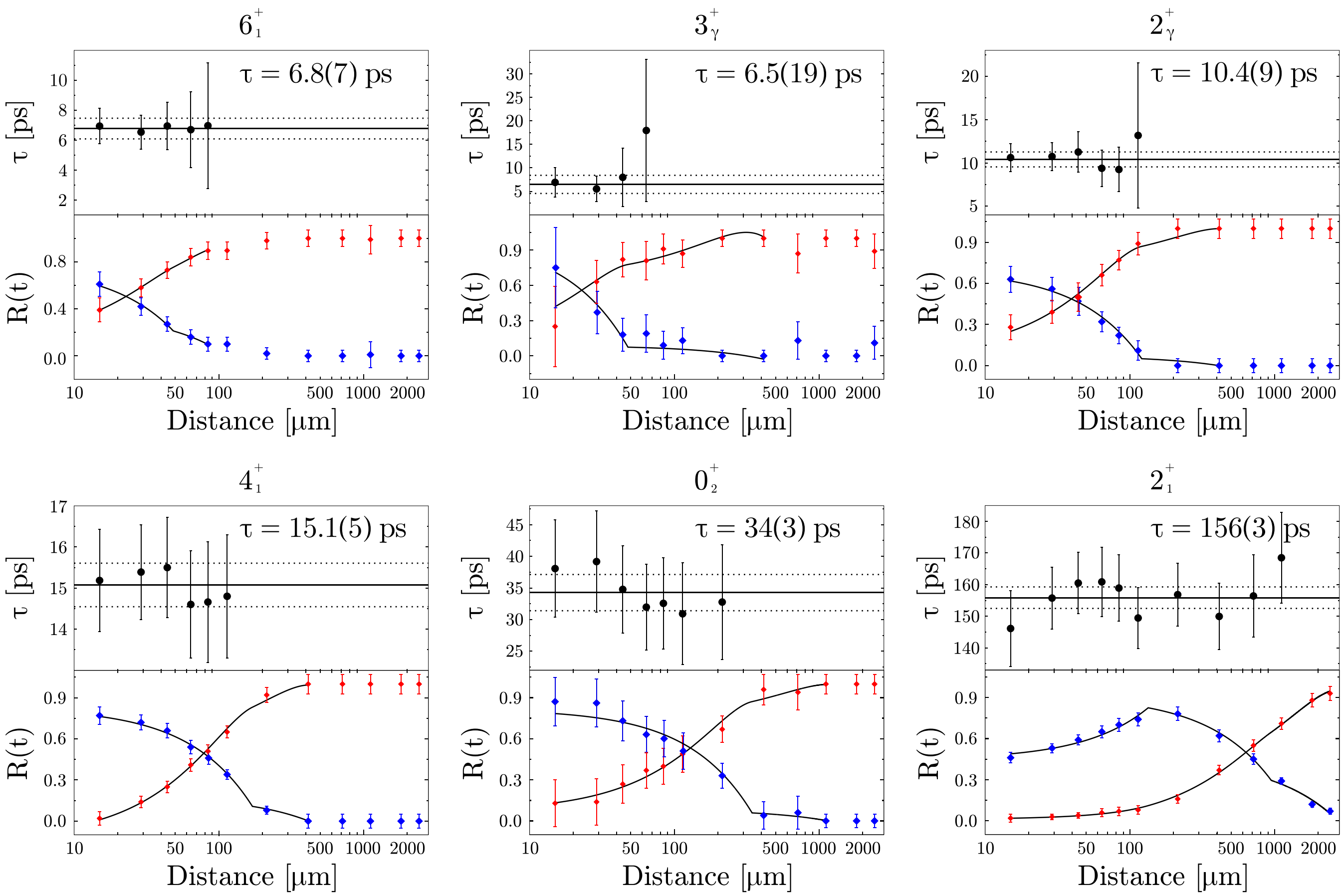

FIG. 5. The DDC method for the 6_1^+, 3_γ^+, 2_γ^+, 4_1^+, 0_2^+, and 2_1^+ states using the program NAPATAU [43] for the backward angle. The upper panel shows the individually obtained lifetimes. The lower panel the evolution of the shifted and unshifted component in addition with a fit which is used to obtain the derivative $\frac{d}{dx}R_i(x)$.

unobserved states (e.g., 8_1^+ state as a feeder of the 6_1^+ state) and other unobserved feeding γ rays, a simulation similar as explained in Sec. III A was performed to account for this. The final results for these states with the inclusion of the feeding contribution are given by $\tau_{6_1^+} = 6.7^{+0.7}_{-3.1}$ ps and $\tau_{3_\gamma^+} = 5.5^{+1.0}_{-3.5}$ ps.

C. The analysis of the 2_1^+, 4_1^+, 0_2^+, and 2_γ^+ states

After the determination of the lifetimes of the higher-lying states, the lifetimes of the lower lying states can be obtained. The shifted and unshifted components of these states are shown in Fig. 3 for four representative distances. All lifetimes have been obtained using the Bateman equations and the DDCM. The decay curves of these states are shown in Fig. 4.

For the 2_γ^+ state, the 551.6 keV transition ($2_\gamma^+ \rightarrow 2_1^+$) was used to determine the lifetime. The second decay transition (848 keV) of this state could not be used due to the $3^- \rightarrow 2_2^+$ (845 keV) transition populated in Coulomb excitation of ^{100}Mo. The evolution of the shifted and unshifted components can be seen in the right panel of Fig. 3. The lifetime was determined for the backward angle detectors but not for the forward angle detectors due to the $2_1^+ \rightarrow 0_1^+$ transition with an energy of 536 keV populated in Coulomb excitation of ^{100}Mo. A possible contamination could be the 550 keV ($4_\gamma^+ \rightarrow 2_\gamma^+$) transition. However, according to the intensities (see Table I), the population of the 4_γ^+ is very low. Furthermore, the lifetime is short ($\tau < 4$ ps) and therefore the effect of this state can be neglected in the analysis procedure. After applying the Bateman equations and the DDCM, the final lifetime is $\tau_{2_\gamma^+} = 10.3(12)$ ps, which is the weighted average of both methods (see Table II).

The $0_2^+ \rightarrow 2_1^+$ transition with 402 keV was used to obtain the lifetime of the 0_2^+ state. The increase of the shifted component with increasing distance is shown in the middle panel of Fig. 3. The weighted average of $\tau_{0_2^+} = 33(4)$ ps is consistent with a former RDDS lifetime measurement with a result of 40(16) ps [47] within the uncertainties.

The evolution of the intensities of the 447 keV ($4_1^+ \rightarrow 2_1^+$) transition is also shown in the middle panel of Fig. 3. A weighted average of $\tau_{4_1^+} = 15.9(12)$ ps is consistent with a former RDDS lifetime measurement [47] that has a result of 18(4) ps. Another lifetime measurement [48] with the result of $\tau_{4_1^+} = 27.8^{+10.5}_{-8.1}$ ps was obtained by the Doppler-shift-attenuation method using a fragment separator in combination with the PreSPEC-AGATA experimental setup [48]. Although the uncertainty of this result is relatively large, it is not consistent with the lifetime value of this work. A reason could be the low statistics of the lifetime determination described in Ref. [48] which makes it difficult to observe possible feeding

TABLE II. Lifetimes measured in the experiment using the Bateman equation (BE), the DDCM method together with the adopted values. The literature values from Refs. [21,47,48] are summarized in the last column.

	Lifetime [ps]					
	Backward ring		Forward ring			
State	BE	DDCM	BE	DDCM	*Adopted*	Lit.
2_1^+	149(6)	156(3)	146(6)	147(3)	*150(10)*	164(19)[a]
						180(6)[b]
						$186.9^{+18.3}_{-18.7}$[c]
4_1^+	18.3(14)	15.1(5)	18.3(20)	16.6(9)	*15.9(12)*	18(4)[a]
						$27.8^{+10.5}_{-8.3}$[c]
6_1^+	6.2(9)	6.8(7)	6.0(9)	7.1(7)	$6.7^{+0.7}_{-3.1}$	3.2(7)[c]
0_2^+	30(6)	34(3)	33(8)	34(3)	*33(4)*	40(16)[a]
2_γ^+	9.9(13)	10.4(9)			*10.3(12)*	
3_γ^+	5.9(18)	6.5(18)	5.2(12)	5.1(11)	$5.5^{+1.0}_{-3.5}$	
4_γ^+	<4				<4	

[a]From Ref. [47].
[b]From Ref. [21].
[c]From Ref. [48].

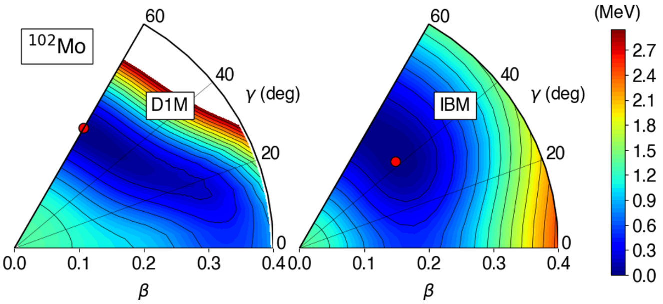

FIG. 6. Contour plot of the deformation-energy surface in the (β, γ) plane for ^{102}Mo computed with the constrained HFB method by using the Gogny functional D1M (left) and with the mapped IBM (right). The red dot indicates the minimum of the energy surface plots and the difference between two neighboring contours is 100 keV.

states of the 4_1^+ other than the 6_1^+ state. Therefore, the possible lifetimes of feeder states could have a significant effect on the lifetime and would possibly lower the value if taken into account during the analysis. The lifetime determination in this experiment benefits from the low level density populated from transfer reactions and the higher statistics (see Fig. 3).

After obtaining the lifetimes of all states above the 2_1^+ state, the lifetime of this state is now accessible and the feeding pattern can be included in its determination. The evolution of the components is shown in the left panel of Fig. 3, and the decay curve in Fig. 4. The lifetimes and intensities of the feeding 0_2^+, 4_1^+, 2_γ^+, 3_γ^+, and 4_γ^+ states are included in the calculation. The final lifetime $\tau_{2_1^+} = 150(10)$ ps is obtained, which is in agreement with a former lifetime measurement with a result of 164(19) ps [47]. Two other lifetimes with 180(6) ps [21] and $186.9^{+18.3}_{-18.7}$ ps [48] are not consistent within the 1σ range.

IV. CALCULATIONS

Calculations using the proton-neutron interacting boson model (IBM-2), where a distinction between proton bosons and neutron bosons is made [49], based on the microscopic energy density functional (EDF), were performed. The parameters of the IBM-2 Hamiltonian are determined by mapping the deformation-energy surface, which is provided by the constrained Gogny-D1M SCMF calculations, onto the expectation value of the IBM Hamiltonian computed with the boson condensate (intrinsic) wave function [37,50]. From the resulting IBM Hamiltonian, energy levels and transition probabilities can be calculated.

The potential-energy surface shown in left part of Fig. 6 exhibits a single minimum. Therefore, only a single configuration of the Hamiltonian in Eq. (2) of Ref. [37] is used. Here only a short description is given and for a more detailed description, the reader is referred to Ref. [37].

To describe ^{102}Mo, the Hamiltonian $\hat{H}_B$ is defined as

$$\hat{H}_B = \epsilon \hat{n}_d + \kappa \hat{Q}_\pi \cdot \hat{Q}_\nu + \kappa' \sum_{\rho' \neq \rho} \hat{T}_{\rho\rho\rho'}, \tag{2}$$

where $\hat{n}_d = \hat{n}_{d\nu} + \hat{n}_{d\pi}$ and $\hat{n}_{d\rho} = d_\rho^\dagger \cdot \tilde{d}_\rho$ $(\rho = \nu, \pi)$ describe the d-boson number operator. The quadrupole operator is defined as $\hat{Q}_\rho = s_\rho^\dagger \tilde{d}_\rho + d_\rho^\dagger \tilde{s}_\rho + \chi_\rho [d_\rho^\dagger \times \tilde{d}_\rho]^{(2)}$ $(\rho = \nu, \pi)$ and the third term is a specific three-boson interaction term with $\hat{T}_{\rho\rho\rho'} = \sum_L [d_\rho^\dagger \times d_\rho^\dagger \times d_{\rho'}^\dagger]^{(L)} \cdot [\tilde{d}_{\rho'} \times \tilde{d}_\rho \times \tilde{d}_\rho]^{(L)}$ with L being the total angular momentum in the boson system. The electromagnetic $E2$ transition rates are calculated via:

$$\hat{T}^{(E2)} = e_B \hat{Q}, \tag{3}$$

where e_b and $\hat{Q}$ are the effective charge and the quadrupole operator, respectively.

The shell closures at $Z = N = 50$ were used to get the boson numbers which are half of the valence protons and neutrons. The ^{102}Mo nucleus is eight protons and ten neutrons away from the closed shell and hence the proton and neutron valence numbers are $N_\pi = 4$ and $N_\nu = 5$, respectively. The adopted Hamiltonian parameters are $\epsilon = 0.66$ MeV, $\kappa = -0.171$ MeV, $\chi_\pi = 0.15$, $\chi_\nu = 0.35$, and $\kappa' = 0.1$ MeV. The effective $E2$ charge is $e_B = 0.141$ eb and the effective g factors are $g_\nu = 0$ for neutrons and $g_\pi = 1$ for protons in units of μ_n.

The mean field and (mapped) IBM potential-energy surfaces (PESs) are shown in Fig. 6. As can be seen, the Gogny-D1M PES displays an oblate minimum around $\beta \approx 0.15$ which was used to obtain the IBM parameters. Note that the Gogny-D1M PES shows two minima in the case of 104, 106 Mo (see Fig. 1 in Ref. [37]). On the right-hand side, the IBM PES shows a minimum around $\beta \approx 0.15$ and a γ deformation of $\gamma \approx 40^\circ$. This can be interpreted as signatures for γ softness in ^{102}Mo, where the maximum γ softness has a very broad minimum at $\gamma = 30^\circ$ spreading to $\gamma = 0^\circ$ (prolate) and $\gamma = 60^\circ$ (oblate).

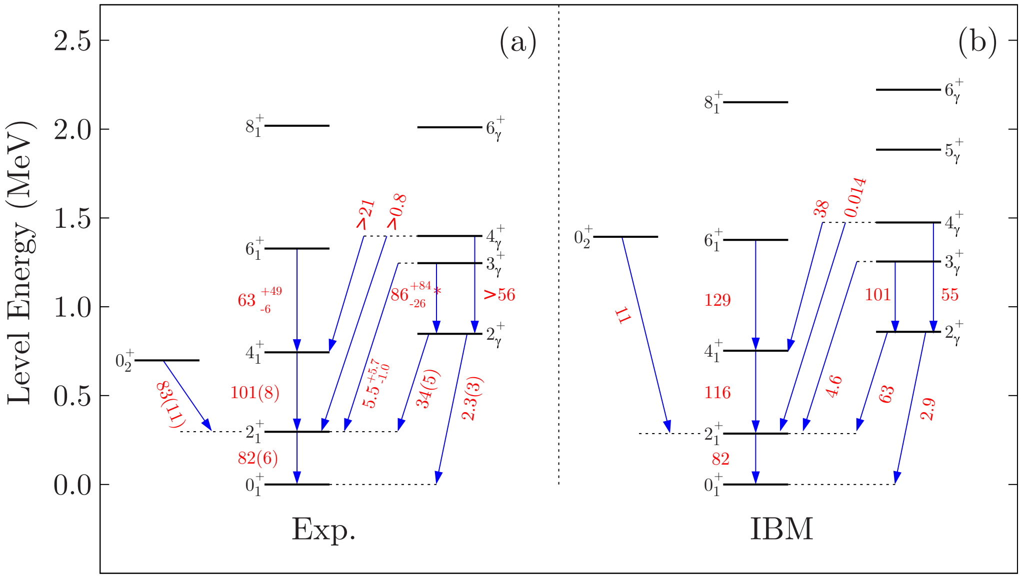

FIG. 7. The level energies of the ground-state band up to the 8_1^+, the γ band up to the 6_γ^+ and the 0_2^+ state which were observed in different experiments (a) and the same level energies for the IBM calculations. The numbers (in red) close to the arrows indicate the $B(E2)$ values in Weisskopf units. The $B(E2; 3_\gamma^+ \rightarrow 2_\gamma^+)$ value indicated with an * is calculated using the limits of a pure $E2$ transition due to a lack of multipole mixing ratios.

V. RESULTS AND DISCUSSION

A. Energy levels

In Fig. 7, the experimental and calculated level energies and transition strengths are shown. The 2_1^+ and 4_1^+ states of the ground-state band are well described by the calculation with an accuracy of 10 keV or better. Although the energy levels of 6_1^+ and 8_1^+ states differ by ≈50 and ≈150 keV, respectively, the IBM is still able to give a reasonable description of these states. The 2_γ^+ bandhead and the 3_γ^+ are described with a difference of less than 10 keV with respect to the experimental observations. The energy level of higher lying states of this band, namely, the 4_γ^+ and 6_γ^+ states, are overestimated by the calculations. The calculations locate the 5_γ^+ state in between the 4_γ^+ and 6_γ^+ state. Three states with level energies of 1617, 1748, and 1870 keV, respectively, could be possible candidates for this proposed 5_γ^+. These states have no adopted spin and lie between the 4_γ^+ and 6_γ^+. They were observed by the β decay of the (4^+) ground state of ^{102}Nb [15] which makes it an allowed β decay to a 5^+ state according to the β-decay selection rules. However, all three states decay to at least one 2^+ state, i.e., 1617 keV → 296 (1250) keV, 1748 keV → 296 keV and 1870 keV → 848 keV. These transitions would imply an $M3/E4$ transition which makes this assignment unlikely. In this case no clear assignment of calculated states to experimental states can be made and further experiments are needed to give a final conclusion. The low-lying 0_2^+ state differs from the calculations by a wide margin, which makes it difficult to interpret this state based on the IBM calculations. A possible explanation for the difference might be that the PES in Fig. 6 shows a pronounced deformation (minimum). This leads to a rotational-like energy spectra with the result of a high 0_2^+ energy level.

B. Reduced transition probabilities

In Fig. 7, the transitions and their respective reduced transition probabilities $B(E2)$ given in Weisskopf units are shown. The corresponding $B(E2)$ and $B(M1)$ values can be found in Table III. Using the microscopic interacting boson approach explained in Sec. IV, the theoretically calculated reduced transition strengths are compared with the experimentally deduced ones. The $B(E2; 2_1^+ \rightarrow 0_1^+)$ fits exactly to the experimental observed reduced transition probability. Going up the yrast band the calculation overestimates the values slightly for the $4_1^+ \rightarrow 2_1^+$ transition and by a factor of two for the $6_1^+ \rightarrow 4_1^+$. Although the experimental uncertainty of the $B(E2; 6_1^+ \rightarrow 4_1^+)$ is high, the calculations are not able to reproduce this value within the error.

The 2_γ^+ state has two decay branches to the 2_1^+ and 0_1^+ state. The $2_\gamma^+ \rightarrow 0_1^+$ transition with an experimental reduced transition probability of 2.3(3) W.u. is overestimated with 2.9 W.u. by the model. The second decay transition $2_\gamma^+ \rightarrow 2_1^+$ with a multipole mixing ratio of $\delta = 7.0^{+1.8}_{-0.6}$ [51] has an overestimated $B(E2)$ value and a $B(M1)$ value that is in good agreement with the calculations. The multipole mixing ratio suggests a predominantly $E2$ type of transition with a more collective nature, which is also supported by the calculation although the value is two times larger with $B(E2) = 63$ W.u.

For the $3_\gamma^+ \rightarrow 2_1^+$ transition, a multipole mixing ratio of $\delta = -9^{+2}_{-3}$ [51] was used. The corresponding $B(E2)$ value is slightly overestimated whereas the $B(M1)$ value is reproduced by the model. For the decay of the 3_γ^+ to the 2_γ^+ state, the multipole mixing ratio is unknown and, therefore, the transition rates are calculated in limits of a pure $E2$ or $M1$ transition. The $B(E2; 3_\gamma^+ \rightarrow 2_\gamma^+)$ is reproduced by the model, while the calculation underestimates the $B(M1; 3_\gamma^+ \rightarrow 2_\gamma^+)$ strength. A multipole mixing ratio of $\delta \approx |19|$ would fit to the calculations

TABLE III. The reduced transition probabilities obtained from the measured lifetimes. The branching ratios are taken from the Nuclear Data Sheets [15]. Due to a lack of $M1/E2$ mixing ratios of some transitions the transition probabilities are calculated by assuming the limits of a pure $E2$ and $M1$ transition, which are marked with *. The $B(E2)$ values are given in W.u. and the $B(M1)$ values are given in $10^{-4}\mu_N^2$.

$J^{\pi 2} \to J^{\pi 1}$	Multipolarity	$B(\sigma\lambda; J^{\pi 2} \to J^{\pi 1})$	IBM
$2_1^+ \to 0_1^+$	$E2$	82(6)	82
$4_1^+ \to 2_1^+$	$E2$	101(8)	116
$6_1^+ \to 4_1^+$	$E2$	63^{+49}_{-6}	129
$0_2^+ \to 2_1^+$	$E2$	83(11)	11
$2_\gamma^+ \to 2_1^+$	$E2$[a]	34(5)	63
	$M1$[a]	$4.2^{+3.4}_{-1.6}$	3.6
$2_\gamma^+ \to 0_1^+$	$E2$	2.3(3)	2.9
$3_\gamma^+ \to 2_1^+$	$E2$[b]	$5.5^{+5.7}_{-1.0}$	4.6
	$M1$[b]	$1.4^{+1.8}_{-0.6}$	2.0
$3_\gamma^+ \to 2_\gamma^+$	$E2$*	86^{+84}_{-26}	101
	$M1$*	270^{+260}_{-80}	0.8
$4_\gamma^+ \to 2_1^+$	$E2$	>0.8	0.014
$4_\gamma^+ \to 2_\gamma^+$	$E2$	>56	55
$4_\gamma^+ \to 4_1^+$	$E2$[c]	>21	38
	$M1$[c]	>29	27
$0_2^+ \to 0_1^+$	$E0$[d]	145(30)[d]	

[a]An $M1/E2$ mixing ratio of $\delta = 7.0^{+1.8}_{-0.6}$ was used [51].
[b]An $M1/E2$ mixing ratio of $\delta = -9^{+2}_{-3}$ was used [51].
[c]An $M1/E2$ mixing ratio of $\delta = 2^{+3}_{-1}$ was used [51].
[d]The electric monopole transitions strength between 0^+ state is given in $10^3 \times \rho^2(E0)$ and were calculated using the method explained in Ref. [52].

for both transitions rates, which would be a dominant $E2$ transition.

Lastly, the $B(E2; 0_2^+ \to 2_1^+) = 83(11)$ W.u. is underestimated by almost one order of magnitude. The overprediction of the energy level and the weak $0_2^+ \to 2_1^+$ transition strength indicate that the 0_2^+ might be of other origin.

C. Shape coexistence

The $E0$ transition probability obtained by the lifetime of the 0_2^+ state indicates shape coexistence, which is widely spread in the $A \approx 100$ region. The $Z \approx 40$ and $N \approx 60$ region is known for the coexistence and mixing of almost spherical and strongly deformed shapes [1,34]. The $\rho(E0)$ values describe the mixing of two states and are indicators for the exhibition of shape coexistence. In the case of small or nonexistent $\rho(E0)$ strengths, the mixing between the states is minimal and sharp mean square radii variations $\Delta\langle r^2\rangle$ are seen. Large $\rho(E0)$ strengths correspond to strong mixing and more gradual mean square radii variations $\Delta\langle r^2\rangle$ (see Figs. 5 and 6 in Ref. [34]). Using the measured lifetime, the obtained $10^3 \times \rho(E0) = 145(30)$ given in Table III is one of the largest values known along the nuclear chart where the ground state is weakly deformed [34,52]. Similar large values were observed in the corresponding isotones ^{100}Zr and ^{98}Sr with $10^3 \times \rho(E0) = 51(5)$ [52,53] and $10^3 \times \rho(E0) = 108(19)$ [52,54,55], respectively. For the higher-Z isotones, namely ^{104}Ru and ^{106}Pd, this large $\rho(E0)$ seems to diminish [1]. However, static and dynamic quadrupole moments in ^{104}Ru show that the shape coexistence still persists [1,56,57]. Going along the isotopic chain of molybdenum isotopes it stands out that the energies of the 0_2^+ states are almost constant for the $N = 56$–62 isotopes, as can be seen in Fig. 8. The same behavior holds for the ruthenium but not for strontium and zirconium isotopes. The strontium and zirconium isotopes show a "V-like" shape with its minimum at $N = 60$ where the well-known shape coexistence is expected. However, the investigation of $E0$ transition probabilities for the $N = 60$ isotones show a clear jump in $\rho^2(E0)$ values for ^{98}Sr, ^{100}Zr and ^{102}Mo (see Fig. 8). The sudden increase of $\rho^2(E0)$ values in the molybdenum isotopes underlines the shape coexisting structure [34]. With values around $10^3 \times \rho^2(E0) \approx 30$, the $N = 56, 58$ molybdenum isotopes possess already relatively large $\rho^2(E0)$ transition probabilities compared with their isotonic partners in the Zr and Ru isotopes, which concentrate in values around 10. The flat behavior of the 0_2^+ energies in molybdenum in combination with the sudden increase of $\rho^2(E0)$ values might be a hint that the shape coexistence is less pronounced. Or in other words that the change in shape evolves more moderate and smooth compared with the strontium and zirconium isotopes. Note that strong mixing is also required to explain the strong $B(E2; 0_2^+ \to 2_1^+)$ transition strength. Also different two-neutron reaction studies reveal that ^{102}Mo exhibits exhibits a coexisting character [1,58–61], which leads to the assumptions of transfer strength to different structures. This underlines the shape coexisting structures in ^{102}Mo and general trend of the $Z \approx 40$ and $N = 60$ isotones.

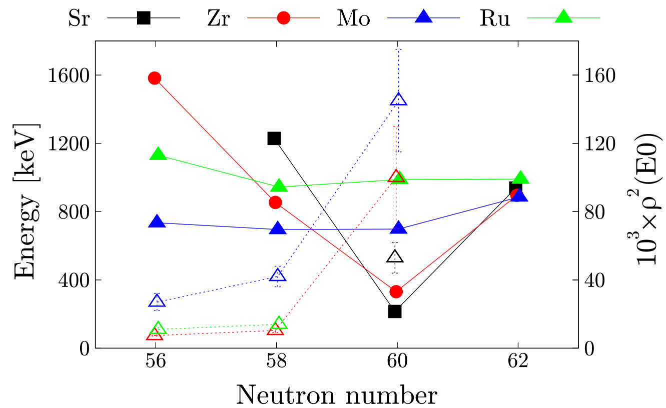

FIG. 8. The energies of the 0_2^+ state (filled symbols) for ($Z = 38$), Zr ($Z = 40$), Mo ($Z = 42$), and Ru ($Z = 44$) isotopes with $N = 56$–62. The data are taken from the Nuclear Data Sheets [11–17]. If available, the $10^3 \times \rho^2(E0)$ are shown for the same isotopes (open symbols), where the data are taken from Refs. [34,52] and for ^{102}Mo from this work. Note that the values are slightly shifted along the x axis to have a better separation of the values.

The IBM calculations could not reproduce the low-lying 0_2^+ state and the strong $0_2^+ \to 2_1^+$ transition strength. The experimental results of this work revealed that the inclusion of shape coexistence should be taken into account to get a more accurate description. A possible approach that has been used for the Zr isotopes might might solve this issue [39,62].

D. γ softness

As seen in Fig. 7, the 2^+_γ level energy lies close to the 4^+_1 state. In the Wilets-Jean γ soft rotor model [30], these states are degenerate, while the Davydov-Filippov rigid triaxial rotor model [27–29] predicts the 2^+_γ state below the 4^+_1 state. To distinguish between those two extreme cases, the staggering parameter is a good indicator and defined as [31]:

$$S(J) = \frac{[E(J) - 2E(J-1) + E(J-2)]}{E(2^+_1)}, \qquad (4)$$

where $E(J)$ represents the energy of the level with spin J in the γ band. The staggering parameter $S(J)$ is negative for even-spin levels and positive for odd-spin levels for a γ-soft nucleus and vice versa for a γ-rigid nucleus. Due to a lack of levels in the γ band, only the $S(4) = -0.83$ is calculated, which is clearly in favor of a γ-soft nucleus. The neighboring ^{100}Mo isotope has $S(4) = -0.91$ and $S(5) = 0.66$ and the ^{104}Mo isotope shows the typical even-odd staggering for a γ-soft nucleus. The IBM calculations further support the γ softness of ^{102}Mo where the energies show the same clustering behavior (see Fig. 7). The resulting potential-energy surface (PES) shows a broad minimum around 40° which has a tendency towards oblate deformation (see Fig. 6).

The deduced transition rates, where the $B(E2; 2^+_\gamma \rightarrow 2^+_1)$ is relatively large and the $B(E2; 2^+_\gamma \rightarrow 0^+_1)$ small, are similar to the γ-soft model and IBM calculations. The transition rates of the 3^+_γ state are in agreement as well with a large $B(E2; 3^+_\gamma \rightarrow 2^+_\gamma)$ and small $B(E2; 3^+_\gamma \rightarrow 2^+_1)$. However, the $B(E2; 3^+_\gamma \rightarrow 2^+_\gamma)$ is calculated within the limits of a pure $E2$ transition. Once the multipole mixing ratio is known the value could be lower.

VI. CONCLUSIONS

The lifetimes of the 2^+_1, 4^+_1, 6^+_1, 0^+_2, 2^+_γ, 3^+_γ, and 4^+_γ states in ^{102}Mo were measured using the RDDS technique. The results were compared with previous measurements and to an IBM calculation which is based on a microscopic energy density functional. All energy levels and transition strengths of the ground state and γ band are described with reasonable accuracy by the model calculation. The shape coexistence in ^{102}Mo has been re-investigated by measuring the lifetime of the 0^+_2 state. The experimental results suggest two coexisting structures which are mixed. Apparently, the microscopic PES fails in ^{102}Mo to predict this property, although it does for ^{104,106}Mo. Furthermore, the deduced transition strengths of the γ band in combination with the energy level reveal signatures a γ-soft behavior. This is supported by the IBM calculation which shows a broad minimum at $\gamma \approx 40°$ that spreads in the γ degree of freedom. The staggering parameter underlines the γ-soft behavior, although only the $S(4)$ has been used. The assignment of the 5^+_γ and level energy of the 7^+_γ would further increase the information about the even-odd staggering. The results show that the description of ^{102}Mo is challenging due to appearance of shape-coexistence and γ softness.

ACKNOWLEDGMENTS

We thank the operator team of the IKP FN Tandem accelerator for the professional support during the experiment. A.E., V.K., and M.B. acknowledge support by the BMBF under Grant No. 05P15PKFNA. G.H. acknowledges support from the ADI-IDEX programm. R.-B.G. acknowledges support by the DFG under Grant No. BL-1513/1-1. The work of K.N. is supported by the Tenure Track Pilot Programme of the Croatian Science Foundation and the École Polytechnique Fédérale de Lausanne, and the Project TTP-2018-07-3554 Exotic Nuclear Structure and Dynamics, with funds of the Croatian-Swiss Research Programme. The Work of L. M. R. is supported by the Spanish Ministry of Economy and Competitiveness (MINECO) Grant No. PGC2018-094583-B-I00.

[1] K. Heyde and J. L. Wood, Rev. Mod. Phys. **83**, 1467 (2011).
[2] P. Cejnar, J. Jolie, and R. F. Casten, Rev. Mod. Phys. **82**, 2155 (2010).
[3] Y. Luo, S. Zhu, J. Hamilton, J. Rasmussen, A. Ramayya, C. Goodin, K. Li, J. Hwang, D. Almehed, S. Frauendorf, V. Dimitrov, J. ye Zhang, X. Che, Z. Jang, I. Stefanescu, A. Gelberg, G. Ter-Akopian, A. Daniel, M. Stoyer, R. Donangelo, J. Cole, and N. Stone, Phys. Lett. B **670**, 307 (2009).
[4] D. Doherty, J. Allmond, R. Janssens, W. Korten, S. Zhu, M. Zielińska, D. Radford, A. Ayangeakaa, B. Bucher, J. Batchelder, C. Beausang, C. Campbell, M. Carpenter, D. Cline, H. Crawford, H. David, J. Delaroche, C. Dickerson, P. Fallon, A. Galindo-Uribarri *et al.*, Phys. Lett. B **766**, 334 (2017).
[5] P. Möller, R. Bengtsson, B. G. Carlsson, P. Olivius, and T. Ichikawa, Phys. Rev. Lett. **97**, 162502 (2006).
[6] I. Stefanescu, A. Gelberg, J. Jolie, P. Van Isacker, P. von Brentano, Y. Luo, S. Zhu, J. Rasmussen, J. Hamilton, A. Ramayya, and X. Che, Nucl. Phys. A **789**, 125 (2007).
[7] P. Singh, R. G. Pillay, J. A. Sheikh, and H. G. Devare, Phys. Rev. C **45**, 2161 (1992).
[8] K. Wrzosek-Lipska, L. Próchniak, M. Zielińska, J. Srebrny, K. Hadyńska-Klęk, J. Iwanicki, M. Kisieliński, M. Kowalczyk, P. J. Napiorkowski, D. Piętak, and T. Czosnyka, Phys. Rev. C **86**, 064305 (2012).
[9] S. Basu and E. Mccutchan, Nucl. Data Sheets **165**, 1 (2020).
[10] C. M. Baglin, Nucl. Data Sheets **113**, 2187 (2012).
[11] D. Abriola and A. Sonzogni, Nucl. Data Sheets **107**, 2423 (2006).
[12] D. Abriola and A. Sonzogni, Nucl. Data Sheets **109**, 2501 (2008).
[13] J. Chen and B. Singh, Nucl. Data Sheets **164**, 1 (2020).
[14] B. Singh and J. Chen, Nucl. Data Sheets **172**, 1 (2021).
[15] D. De Frenne, Nucl. Data Sheets **110**, 1745 (2009).
[16] J. Blachot, Nucl. Data Sheets **108**, 2035 (2007).
[17] D. De Frenne and A. Negret, Nucl. Data Sheets **109**, 943 (2008).
[18] J. Blachot, Nucl. Data Sheets **62**, 803 (1991).

[19] S. Raman, C. Nestor, and P. Tikkanen, At. Data Nucl. Data Tables **78**, 1 (2001).

[20] P. F. Mantica, A. E. Stuchbery, D. E. Groh, J. I. Prisciandaro, and M. P. Robinson, Phys. Rev. C **63**, 034312 (2001).

[21] M. Liang, H. Ohm, B. De Sutter, K. Sistemich, B. Fazekas, and G. Molnar, Z. Phys., A Hadrons Nucl. **340**, 223 (1991).

[22] J. Ha, T. Sumikama, F. Browne, N. Hinohara, A. M. Bruce, S. Choi, I. Nishizuka, S. Nishimura, P. Doornenbal, G. Lorusso, P.-A. Söderström, H. Watanabe, R. Daido, Z. Patel, S. Rice, L. Sinclair, J. Wu, Z. Y. Xu, A. Yagi, H. Baba, N. Chiga *et al.*, Phys. Rev. C **101**, 044311 (2020).

[23] R. Rodríguez-Guzmán, P. Sarriguren, L. Robledo, and S. Perez-Martin, Phys. Lett. B **691**, 202 (2010).

[24] A. G. Smith, J. L. Durell, W. R. Phillips, W. Urban, P. Sarriguren, and I. Ahmad, Phys. Rev. C **86**, 014321 (2012).

[25] H. Hua, C. Y. Wu, D. Cline, A. B. Hayes, R. Teng, R. M. Clark, P. Fallon, A. Goergen, A. O. Macchiavelli, and K. Vetter, Phys. Rev. C **69**, 014317 (2004).

[26] R. F. Casten, *Nuclear Structure from a Simple Perspective*, Oxford Studies in Nuclear Physics (Oxford University Press, Oxford, 2000).

[27] A. Davydov and G. Filippov, Nucl. Phys. **8**, 237 (1958).

[28] A. Davydov and V. Rostovsky, Nucl. Phys. **12**, 58 (1959).

[29] A. Davydov and V. Rostovskii, J. Expt. Theor. Phys. (USSR) **36**, 1788 (1959) [Sov. Phys. JETP **36**, 1275 (1959)].

[30] L. Wilets and M. Jean, Phys. Rev. **102**, 788 (1956).

[31] N. Zamfir and R. Casten, Phys. Lett. B **260**, 265 (1991).

[32] E. A. McCutchan, D. Bonatsos, N. V. Zamfir, and R. F. Casten, Phys. Rev. C **76**, 024306 (2007).

[33] P. E. Garrett, J. Phys. G **27**, R1 (2000).

[34] J. Wood, E. Zganjar, C. De Coster, and K. Heyde, Nucl. Phys. A **651**, 323 (1999).

[35] T. Thomas, K. Nomura, V. Werner, T. Ahn, N. Cooper, H. Duckwitz, M. Hinton, G. Ilie, J. Jolie, P. Petkov, and D. Radeck, Phys. Rev. C **88**, 044305 (2013).

[36] M. Zielińska, T. Czosnyka, J. Choiński, J. Iwanicki, P. Napiorkowski, J. Srebrny, Y. Toh, M. Oshima, A. Osa, Y. Utsuno, Y. Hatsukawa, J. Katakura, M. Koizumi, M. Matsuda, T. Shizuma, M. Sugawara, T. Morikawa, H. Kusakari, A. Efimov, and V. Mikhajlov, Nucl. Phys. A **712**, 3 (2002).

[37] K. Nomura, R. Rodríguez-Guzmán, and L. M. Robledo, Phys. Rev. C **94**, 044314 (2016).

[38] A. Dewald, O. Möller, and P. Petkov, Prog. Part. Nucl. Phys. **67**, 786 (2012).

[39] V. Karayonchev, J. Jolie, A. Blazhev, A. Dewald, A. Esmaylzadeh, C. Fransen, G. Häfner, L. Knafla, J. Litzinger, C. Müller-Gatermann, J.-M. Régis, K. Schomacker, A. Vogt, N. Warr, A. Leviatan, and N. Gavrielov, Phys. Rev. C **102**, 064314 (2020).

[40] A. Esmaylzadeh, V. Karayonchev, G. Häfner, J. Jolie, M. Beckers, A. Blazhev, A. Dewald, C. Fransen, A. Goldkuhle, L. Knafla, and C. Müller-Gatermann, Phys. Rev. C **103**, 054324 (2021).

[41] M. Beckers, C. Müller-Gatermann, A. Blazhev, T. Braunroth, A. Dewald, C. Fransen, A. Goldkuhle, L. Kornwebel, J. Litzinger, F. von Spee, and K.-O. Zell, Phys. Rev. C **102**, 014324 (2020).

[42] T. Alexander and A. Bell, Nucl. Instrum. Methods **81**, 22 (1970).

[43] B. Saha, Ph.D. thesis, Universität zu Kön, 2004 (unpublished).

[44] H. Bateman, Proc. Cambridge Philos. Soc. **15**, 423 (1910).

[45] A. Dewald, S. Harissopulos, and P. von Brentano, Z. Phys. At. Nucl. 334, 163 (1989).

[46] J. Litzinger, A. Blazhev, A. Dewald, F. Didierjean, G. Duchêne, C. Fransen, R. Lozeva, K. Sieja, D. Verney, G. de Angelis, D. Bazzacco, B. Birkenbach, S. Bottoni, A. Bracco, T. Braunroth, B. Cederwall, L. Corradi, F. C. L. Crespi *et al.*, Phys. Rev. C **92**, 064322 (2015).

[47] H. Bohn, P. Kienle, D. Proetel, and R. L. Hershberger, Z. Phys. At. Nucl. **274**, 327 (1975).

[48] D. Ralet, S. Pietri, T. Rodríguez, M. Alaqeel, T. Alexander, N. Alkhomashi, F. Ameil, T. Arici, A. Ataç, R. Avigo, T. Bäck, D. Bazzacco, B. Birkenbach, P. Boutachkov, B. Bruyneel, A. M. Bruce, F. Camera, B. Cederwall, S. Ceruti, E. Clément, M. L. Cortés, D. Curien *et al.* (PreSPEC and AGATA Collaborations), Phys. Rev. C **95**, 034320 (2017).

[49] F. Iachello and A. Arima, in *The Interacting Boson Model*, Cambridge Monographs on Mathematical Physics (Cambridge University Press, Cambridge, 1987).

[50] J. Ginocchio and M. Kirson, Nucl. Phys. A **350**, 31 (1980).

[51] J. M. Eldridge, B. Fenker, J. H. Hamilton, C. Goodin, C. J. Zachary, E. Wang, A. V. Ramayya, A. V. Daniel, G. M. Ter-Akopian, Y. T. Oganessian, Y. X. Luo, J. O. Rasmussen, and S. J. Zhu, Eur. Phys. J. A **54**, 15 (2018).

[52] T. Kibédi and R. Spear, At. Data Nucl. Data Tables **89**, 77 (2005).

[53] F. Schussler, J. Pinston, E. Monnand, A. Moussa, G. Jung, E. Koglin, B. Pfeiffer, R. Janssens, and J. van Klinken, Nucl. Phys. A **339**, 415 (1980).

[54] T. A. Khan, W. D. Lauppe, K. Sistemich, H. Lawin, G. Sadler, and H. A. Selic, Z. Phys. A **283**, 105 (1977).

[55] F. K. Wohn, J. C. Hill, C. B. Howard, K. Sistemich, R. F. Petry, R. L. Gill, H. Mach, and A. Piotrowski, Phys. Rev. C **33**, 677 (1986).

[56] L. Svensson, C. Fahlander, L. Hasselgren, A. Bäcklin, L. Westerberg, D. Cline, T. Czosnyka, C. Wu, R. Diamond, and H. Kluge, Nucl. Phys. A **584**, 547 (1995).

[57] J. Srebrny, T. Czosnyka, C. Droste, S. Rohoziński, L. Próchniak, K. Zajac, K. Pomorski, D. Cline, C. Wu, A. Bäcklin, L. Hasselgren, R. Diamond, D. Habs, H. Körner, F. Stephens, C. Baktash, and R. Kostecki, Nucl. Phys. A **766**, 25 (2006).

[58] R. Casten, E. Flynn, O. Hansen, and T. Mulligan, Nucl. Phys. A **184**, 357 (1972).

[59] E. R. Flynn, F. Ajzenberg-Selove, R. E. Brown, J. A. Cizewski, and J. W. Sunier, Phys. Rev. C **24**, 2475 (1981).

[60] E. R. Flynn, R. E. Brown, J. A. Cizewski, J. W. Sunier, W. P. Alford, E. Sugarbaker, and D. Ardouin, Phys. Rev. C **22**, 43 (1980).

[61] M. A. Rahman and M. S. Chowdhury, Phys. Rev. C **73**, 054311 (2006).

[62] N. Gavrielov, A. Leviatan, and F. Iachello, Phys. Rev. C **99**, 064324 (2019).